**Research Article**

# Interfacial energy barrier tuning of hierarchical Bi₂O₃/WO₃ heterojunctions for advanced triethylamine sensor

Mingxin ZHANG[†], Kai LIU[†], Xingmin ZHANG, Bingbing WANG,
Xinru XU, Xinxin DU, Chao YANG, Kewei ZHANG[*]

*College of Materials Science and Engineering, State Key Laboratory of Bio-Fibers and Eco-Textiles,
Collaborative Innovation Center for Marine Biomass Fibers, Materials and Textiles of
Shandong Province, Qingdao University, Qingdao 266071, China*

**Abstract:** Traditional triethylamine (TEA) sensors suffer from the drawback of serious cross-sensitivity due to the low charge-transfer ability of gas-sensing materials. Herein, an advanced anti-interference TEA sensor is designed by utilizing interfacial energy barriers of hierarchical Bi₂O₃/WO₃ composite. Benefiting from abundant slit-like pores, desirable defect features, and amplification effect of heterojunctions, the sensor based on Bi₂O₃/WO₃ composite with 40% Bi₂O₃ (0.4-Bi₂O₃/WO₃) demonstrates remarkable performance in terms of faster response/recovery time (1.7-fold/1.2-fold), higher response (2.1-fold), and lower power consumption (30 ℃-decrement) as compared with the pristine WO₃ sensor. Furthermore, the composite sensor exhibits long-term stability, reproducibility, and negligible response towards interfering molecules, indicating the promising potential of Bi₂O₃/WO₃ heterojunctions in anti-interference detection of low-concentration TEA in real applications. This work not only offers a rational solution to design advanced gas sensors by tuning the interfacial energy barriers of heterojunctions, but also provides a fundamental understanding of hierarchical Bi₂O₃ structures in the gas-sensing field.

**Keywords:** Bi₂O₃/WO₃; heterojunctions; hierarchical structures; triethylamine (TEA); gas sensors

## 1  Introduction

Triethylamine (TEA), known as one of the most common volatile organic compounds (VOCs), not only easily causes open fire and explosions, but also brings great damage to human dermal, ocular, and respiratory system due to its corrosivity and toxicity [1–3]. According to the permissible exposure degrees stipulated by the Occupational Safety and Health Administration (OSHA), the threshold value of toxic TEA concentration that humans can tolerate is 10 ppm [4–6]. The TEA is also a sort of quite important industrial raw materials that served as organic solvents, synthetic dyes, and catalysts in organic synthesis, especially as a noteworthy biomarker of the decomposition from fish and other seafood [7,8]. Ref. [9] has shown that the TEA released from 200 g of putrid crucian for 7 d is less than 4 ppm, reflecting significant potential in freshness detection of seafood. Traditional TEA detection methods such as chromatography and colorimetry are limited due to their

---

† Mingxin Zhang and Kai Liu contributed equally to this work.

* Corresponding author.

E-mail: zhkw@qdu.edu.cn

high cost and cumbersome detection procedures [10–12]. Therefore, reliable TEA sensors with high response, low cost, and convenient operation are required for promising applications in industrial production, food safety, and human health. In addition, the traditional TEA sensors still suffer from the drawback of serious cross-sensitivity, mainly due to low charge-transfer ability of gas-sensing materials.

Metal oxide semiconductors (MOSs) have been widely used in the gas sensors due to their attractive physical and chemical properties [13–15]. Generally, a semiconductor gas sensor is composed of a receptor function and a transducer function, which recognizes the adsorption and reaction of target gases on a sensing layer. The change in the electrical resistance of the sensing materials is recorded as a sensor signal. Among various MOSs, tungsten oxide ($WO_3$) demonstrates high sensitivity, fast response, and long-term stability towards various gas species, owing to its non-toichiometry and chemical diversity [16]. However, the high activation energy for the chemisorption results in relatively high operating temperatures of $WO_3$-based sensors. The formation of the heterojunctions and the heterogeneous structures has definitely proved that they can improve the sensing behavior of the MOSs [17–19]. As reported in Refs. [20,21], the valence bands of $WO_3$ and bismuth oxide ($Bi_2O_3$) are 3.44 and 3.13 eV, respectively. Thus, the holes on the valence bands of both $WO_3$ and $Bi_2O_3$ have a strong oxidative capability that is similar to $TiO_2$, making them attractive for photocatalytic applications. Recently, the heterojunction between $Bi_2O_3$ and $WO_3$ has attracted special attention for photodegradation and water splitting. Wei *et al*. [22] designed the porous $WO_3$ microspheres embedded with $Bi_2O_3$ nanosheets, facilitating the separation and migration of charge carriers for dye photodegradation. Khan *et al*. [23] synthesized $Bi_2O_3$/h-$WO_3$ nanocomposite as photoactive materials for water splitting, which exhibited a decreased bandgap and minimized recombination of the charge carriers due to the strain effect of $Bi_2O_3$. As is well known, the adsorption and reaction behavior of the target gases on the gas-sensing materials has relations with the catalytic process. From the viewpoint of the accessible materials, $Bi_2O_3$ possesses advantages of tunable electrical conductivity and high electron affinity [24]. Although pure $Bi_2O_3$ is rarely used for the gas-sensing purpose due to its slow electronic mobility at low temperatures [25], it was reported that the $Bi_2O_3$/$SnO_2$ materials are sensitive to CO due to the

participation of the $Bi_2Sn_2O_7$ phase [26]. The $Bi_2O_3$/$WO_3$ heterogeneous materials thus show great potential to achieve reliable gas sensors, and more related research is needed to explore.

In this work, we design an advanced TEA sensor by utilizing the interfacial energy barriers of the hierarchical $Bi_2O_3$/$WO_3$ composite. The composite was prepared through the hydrothermal–ultrasonic combination procedure followed by thermal treatment. On the basis of the hierarchical $Bi_2O_3$/$WO_3$ composite, the designed sensor possesses a high response of the TEA of 9.2–50 ppm at a low temperature of 140 ℃. The response and recovery time are 1.7-fold and 1.2-fold, respectively, as compared with those of the pristine $WO_3$ sensor. Furthermore, the composite sensor exhibits long-term stability, reproducibility, and negligible response towards the interfering molecules, indicating its potential application for anti-interference detection of the low-oncentration TEA. Herein, the superior TEA-sensing performance is attributed to abundant slit-like pores, desirable defect features, and amplification effect of the heterojunctions between $WO_3$ and $Bi_2O_3$. The presented work offers an easy solution for the rational design of other binary MOS sensors by utilizing the interfacial energy barriers of hierarchical metal oxides.

## 2 Experimental

### 2. 1 Preparation of hierarchical $Bi_2O_3$

In a typical process, $Bi(NO_3)_3$ of 0.97 g was dissolved in a mixture of ethanol of 34 mL and ethylene glycol of 17 mL under magnetic stirring at room temperature to form a uniform transparent solution. After stirring for 30 min, the resulting solution was transferred into a Teflon-lined stainless-steel autoclave of 50 mL and heated at 160 ℃ for 5 h. The white precipitates were collected by centrifugation, washed with ethanol for several cycles, and then dried in an oven at 60 ℃ for 8 h.

### 2. 2 Preparation of hierarchical $WO_3$ and $Bi_2O_3$/$WO_3$ composites

Hierarchical $WO_3$·$H_2O$ was prepared via rapid sonochemical method [27]. Typically, $Na_2WO_4$·$2H_2O$ of 3.912 g and oxalic acid of 1.500 g were dissolved in deionized water of 48 mL with stirring at room temperature for 20 min. Then, certain amounts of 3 M HCl solution were added dropwise to the clear solution.

After sonicating for 1 h, the resulting $WO_3 \cdot H_2O$ precipitates were washed with deionized water several times followed by drying overnight. The as-synthesized $WO_3 \cdot H_2O$ was dehydrated and transformed into anhydrous $WO_3$ during the subsequent thermal treatment. A sequence of the hierarchical $Bi_2O_3/WO_3$ composite was then prepared by mixing hierarchical $Bi_2O_3$ and $WO_3$ with different $Bi_2O_3$ molar ratios. When the $Bi_2O_3$ contents are 20%, 40%, 60%, and 80%, the composites are labelled as 0.2-$Bi_2O_3/WO_3$, 0.4-$Bi_2O_3/WO_3$, 0.6-$Bi_2O_3/WO_3$, and 0.8-$Bi_2O_3/WO_3$, respectively.

### 2. 3 Characterization

The crystal phases and morphologies of the samples were studied by an X-ray diffractometer (DX2700, Dandong Haoyuan Instrument Co., Ltd.) and a scanning electron microscope (SEM; 250 FEG, Quanta) attached with energy dispersive spectroscopy (EDS). The specific surface area of the 0.4-$Bi_2O_3/WO_3$ sample was characterized with a Brunauer–Emmett–Teller (BET) analyzer (Autosorb-iQ2, Quantachrome). Thermogravimetric (TG) analysis was carried out in a dynamic air atmosphere by a TG analyzer (STA 449 F5 Jupiter, Netzsch). Raman spectra were acquired by a Raman spectrometer (HR800, Horiba), which was performed with an excitation wavelength of 785 nm. X-ray photoelectron spectroscopy (XPS) results were taken by an X-ray spectrometer (Escalab 250Xi+, Thermo Fisher). Ultraviolet–visible (UV–Vis) spectra were recorded with a spectrophotometer (U-3900H, Hitachi) with an integrating sphere. Photoluminescence (PL) spectra were determined by a spectrofluorometer (Fluoro-max-4, Horiba).

### 2. 4 Fabrication and gas-sensing test of sensors

The fabrication of the gas sensor was divided into several steps. Firstly, the as-prepared samples of 1 mg and terpineol (binding agent) of several microliters were ground in an agate mortar for 5 min to form a uniform slurry. The obtained slurry was slowly and evenly coated on a commercial Ag/Cr interdigital electrode by spinning at 2000 r/min for 15 s. As shown in Fig. S1(a) in the Electronic Supplementary Material (ESM), a successive gas-sensing layer on the surface of the interdigital electrode was formed after annealing at 400 ℃ for 2 h. Finally, the sensor element was aged at 200 ℃ for 10 h to improve the stability and repeatability. The sensor resistance in air ($R_0$) or target gas ($R_g$) was tested under a direct current (DC) bias voltage of 3 V in a homemade chamber connected with a computer-controlled sourcemeter (2612B, Keithley), as shown in Fig. S1(b) in the ESM. The response value of the gas sensor is calculated by the expression of $R_0/R_g$ for the reducing gas. Moreover, the response and recovery time are defined as the time required for the sensor to reach 90% of the total variation values.

## 3 Results and discussion

As shown in Fig. 1(a), the hierarchical $WO_3$ and $Bi_2O_3$ architectures were prepared through the hydrothermal and ultrasonic procedures, respectively, and the hierarchical $Bi_2O_3/WO_3$ composite was obtained after the mixing and thermal treatment. The formation process of the hierarchical $WO_3$ architectures can be explained by the ultrasonic cavitation and Ostwald ripening [28]. At the initial stage of the reaction, oxalic acid is considered as the chelating agent to control the nucleation rate and slow down the sol–gel process in an aqueous solution. After that, the colorless $WO_4^{2-}$ ions are transformed into a yellow $H_2WO_4$ precursor. In the ultrasonic process, the nucleophilic addition reaction between the water molecule and the $H_2WO_4$ molecule results in the formation of hexagonal $WO(OH)_4(H_2O)$ octahedra. Due to the mono-oxo coordination nature of $W^{6+}$, each W atom is connected by four bridging oxygens (OH) in the *XY* plane, one terminal oxygen W=O in the *Z* axis, and one water molecule by hydrogen bonds at the symmetric position of W=O bonds. This octahedral structure easily forms a lamellar structure in the *XY* plane through a co-angular polycondensation reaction, and water molecules are located between these lamellas. Finally, the $WO(OH)_4(H_2O)$ lamellas were reassembled by edge-tacking along the *Z* axis under dipole interaction, and the hierarchical $WO_3 \cdot H_2O$ was formed, which was further dehydrated and transformed into anhydrous $WO_3$ after the heat treatment. For the formation of the hierarchical $Bi_2O_3$ architectures, numerous $Bi_2O_3$ nanocrystals nucleate from the solution and aggregate into nanosheets. Under the tendency of thermodynamic stability, the formed $Bi_2O_3$ nanosheets rearrange themselves and stack with each other to form the hierarchical architectures. The hierarchical $WO_3 \cdot H_2O$ and $Bi_2O_3$ architectures were mixed with the assistance of terpineol to form pastes, and then coated onto the commercial Ag/Cr interdigital electrode by spinning at

2000 r/min for 15 s. After drying, it was calcined at 400 ℃ for 2 h to get good stability and remove the terpineol on the interdigital electrode. Herein, the calcination temperature was determined from the TG analysis of the composite (Fig. S2 in the ESM), where a major mass loss is observed at the temperature ranging from 100 to 350 ℃ due to the loss of chemically bonded water from $WO_3 \cdot H_2O$ and the decomposition of residual carboxylate in the composite. Figures 1(b)–1(d) and Fig. S3 in the ESM show the SEM images of the pure $WO_3$, pure $Bi_2O_3$, and the $Bi_2O_3/WO_3$ composite with different $Bi_2O_3$ ratios after calcination at 400 ℃. Differently from the hierarchical $Bi_2O_3$ (Fig. 1(c)), the sintering growth of the hierarchical $WO_3$ under the calcination is observed (Fig. 1(b)). In the 0.4-$Bi_2O_3/WO_3$ composite (Fig. 1(d)), the nanosheet-assembled $WO_3$ microspheres (2–3 mm) are separated by nanosheet-assembled $Bi_2O_3$ microspheres (4–6 mm). Besides, the addition of $Bi_2O_3$ significantly suppressed the Ostwald ripening of the $WO_3$ microspheres during the calcination, resulting in smaller sizes of the $WO_3$

microspheres in the $Bi_2O_3/WO_3$ composite. The EDS analysis confirms the homogeneity of W, Bi, and O elements in the whole 0.4-$Bi_2O_3/WO_3$ composite (Fig. 1(e)). The porous structure of the 0.4-$Bi_2O_3/WO_3$ composite was confirmed by the nitrogen adsorption–desorption isotherms. As shown in Fig. S4 in the ESM, the isotherms exhibit a type-H3 hysteresis loop, suggesting the existence of slit-like pores in the hierarchical composite. The specific surface area of the 0.4-$Bi_2O_3/WO_3$ sample was calculated to be 50.98 $m^2$/g by the BET method.

To investigate the phase structure, crystallinity, and composition, X-ray diffraction (XRD) patterns were collected for the $Bi_2O_3$, $WO_3$, and $Bi_2O_3/WO_3$ samples, as shown in Fig. 2(a) and Fig. S5 in the ESM. For the hierarchical $Bi_2O_3$, the smooth and sharp diffraction peaks can be indexed to the monoclinic α-$Bi_2O_3$ (JCPDS No. 71-2274) [29]. For the hierarchical $WO_3$, the three overwhelming diffraction peaks with $2\theta$ = 23.12°, 23.59°, and 24.38° corresponded to the (002), (020), and (002) planes of $WO_3$ (JCPDS No. 43-1035) [30], respectively. For the hierarchical $Bi_2O_3/WO_3$
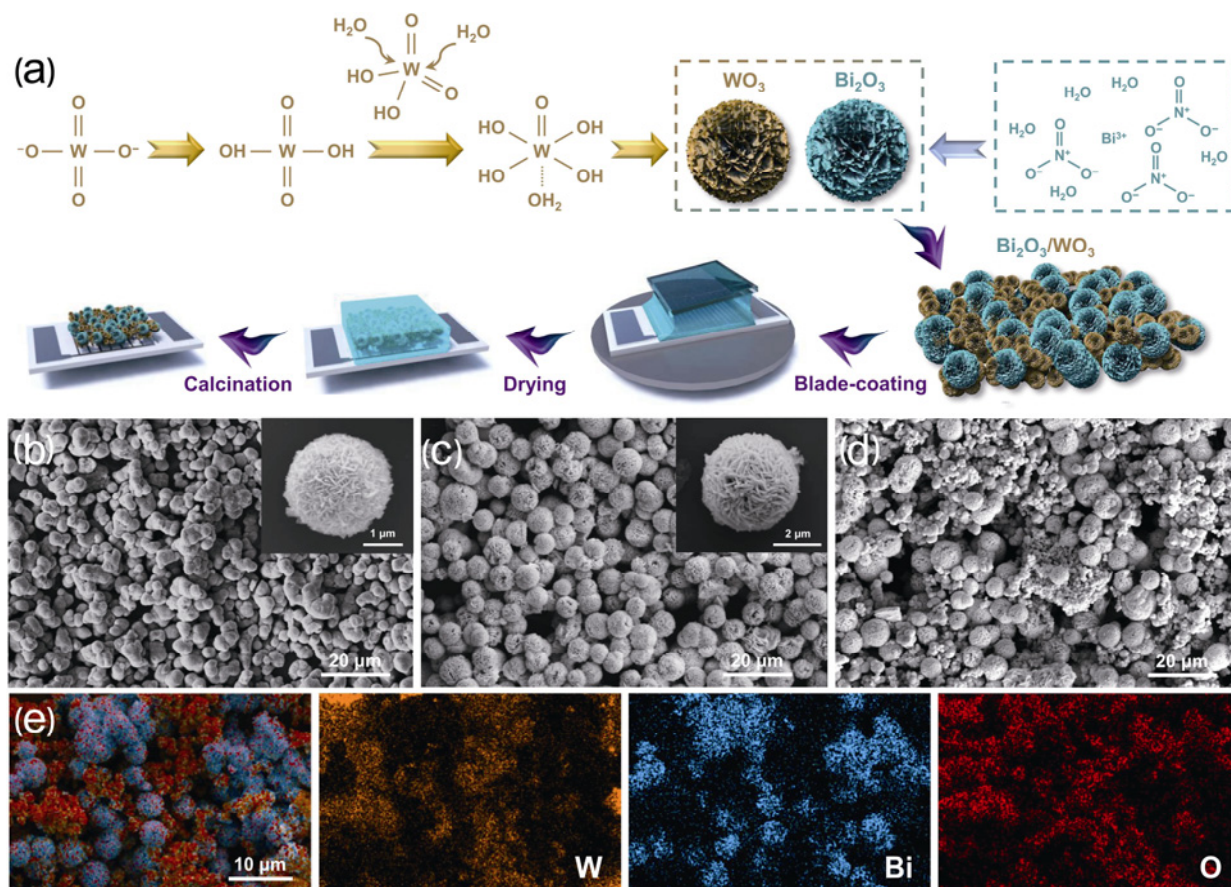


**Fig. 1**  (a) Schematic illustration of preparation of hierarchical $WO_3$, $Bi_2O_3$, and $Bi_2O_3/WO_3$ composites and the corresponding gas sensors. SEM images of (b) hierarchical $WO_3$, (c) $Bi_2O_3$, and (d) 0.4-$Bi_2O_3/WO_3$. (e) Elemental mappings of hierarchical 0.4-$Bi_2O_3/WO_3$ composite, showing W, Bi, and O distributions.

composite, all the diffraction peaks belonging to $Bi_2O_3$ and $WO_3$ can be observed, suggesting the mixed phases of $Bi_2O_3$ and $WO_3$ in the composite. The Raman peaks at 184, 260, 312, 703, 801, and 954 $cm^{-1}$ are consistent with monoclinic $WO_3$ [31]. For the pure $Bi_2O_3$, the characteristic Raman peaks from 100 to 500 $m^{-1}$ are in good agreement with monoclinic $\alpha$-$Bi_2O_3$ [32]. All the characteristic peaks of $WO_3$ and $Bi_2O_3$ are obviously present in the Raman spectrum of $Bi_2O_3$/$WO_3$ composite curves (Fig. 2(b)), suggesting the formation of the $Bi_2O_3$/$WO_3$ composite with no impurities. Along with the increase of $Bi_2O_3$ content in the composite, the relative intensity of the characteristic peaks from $WO_3$ decreases, and the relative intensity of the characteristic peaks from $Bi_2O_3$ increases (Fig. S6 in the ESM). Herein, the slight variations in the position, width, and relative intensity of these characteristic peaks are observed, which may be ascribed to the slight structural variations and sample shape of the $Bi_2O_3$/$WO_3$ composite, as compared with those of the pristine $Bi_2O_3$ and $WO_3$. Figure 2(c) compares the UV–Vis absorption spectra of the as-prepared materials, in which the $WO_3$ and $Bi_2O_3$ have similar absorption edges at 450–500 nm, whereas the $Bi_2O_3$/$WO_3$ composite shows an absorption edge at around 567 nm. In general, the optical band gaps ($E_g$) of the semiconductors can be calculated from the

absorbance data according to Eq. (1):

$$\alpha h v = A(h v - E_g)^n \qquad (1)$$

where $\alpha$, $h$, $v$, and $A$ are the absorption coefficient, the Planck constant, the light frequency, and a constant, respectively, and $n = 0.5$ for the allowed direct transition. From the intersection of the tangent line of the curve, extrapolated to the $hv$-axis intercept, the band gaps of $Bi_2O_3$, $WO_3$, and $Bi_2O_3$/$WO_3$ composites were estimated to be 2.83, 2.78, and 2.42 eV, respectively (the inset in Fig. 2(c)). As compared with those of single components, the decreased band gap of the $Bi_2O_3$/$WO_3$ composite may be attributed to the formation of defects and impurity energy levels within the forbidden band gap [33].

In order to further investigate the surface chemical compositions and chemical states, the XPS studies were carried out for the obtained samples. As shown in Fig. 2(d), two oxidation states of $W^{6+}$ and $W^{5+}$ exist in the $WO_3$ and $Bi_2O_3$/$WO_3$ samples. The dominant chemical state of W is $W^{6+}$ in the samples, which displays the highest binding energy peak [34]. The existence of $W^{5+}$ atom proves that there are considerable amounts of defects in the crystal structure of $WO_3$. Figure 2(e) exhibits that both $Bi_2O_3$ and $Bi_2O_3$/$WO_3$ composites have the same peaks at 158.8 and 164.2 eV, which can correspond to the Bi $4f_{5/2}$ and $4f_{7/2}$ spectra of $Bi^{3+}$,
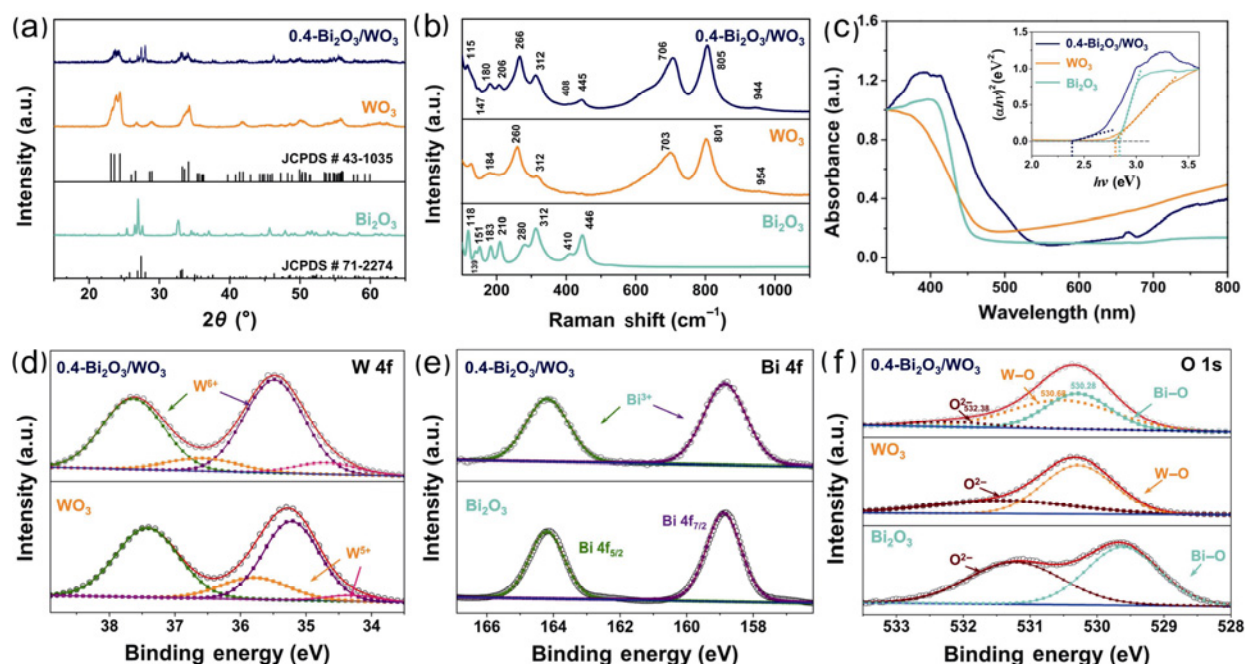
**Fig. 2** (a) XRD patterns, (b) Raman spectra, and (c) UV–Vis absorbance spectra of $Bi_2O_3$, $WO_3$, and 0.4-$Bi_2O_3$/$WO_3$. The inset in (c) shows the calculated band gap values. High-resolution XPS spectra showing (d) W 4f and (e) Bi 4f of $WO_3$ and 0.4-$Bi_2O_3$/$WO_3$, and (f) O 1s of $Bi_2O_3$, $WO_3$, and 0.4-$Bi_2O_3$/$WO_3$.

respectively [35]. In the O 1s spectra (Fig. 2(f)), the binding energies of 530.68, 530.28, and 532.38 eV are attributed to the W–O bond, Bi–O bond, and lattice oxygen, respectively. As compared with those of $Bi_2O_3$ and $WO_3$, obvious shifts of the XPS spectra are observed for the $Bi_2O_3/WO_3$ composite, reflecting a change in the local environment and electronic properties of surface atoms caused by the heterojunction. This result further demonstrates the co-existence of $WO_3$ and $Bi_2O_3$ in the composite, which is in agreement with the SEM (Fig. 1), XRD (Fig. 2(a)), and Raman (Fig. 2(b)) results.

For semiconductor materials, when the electrons or defects of the transitions migrate to a higher energy level, and then return to the ground state after illumination excitation, they will emit certain characteristic spectra. Therefore, the PL is an effective means to study the defects of semiconductors [36]. Figure 3(a) shows that all the obtained samples present luminescence in both the ultraviolet and the visible regions, which may be caused by the photoexcited electron–hole pairs or intrinsic defects. Figures 3(b)–3(d) show the defect-related luminescence of the PL spectra obtained by Gaussian fitting for the $WO_3$, $Bi_2O_3$, and $Bi_2O_3/WO_3$ samples. As is well known, near-band-edge (NBE) emission in the ultraviolet region is caused by the inter-band transitions and exciton recombination, while

deep level (DL) emission in the visible region is caused by a shift in the subcenter of the laser in the deep energy level. The DL is associated with the defects such as oxygen vacancies and interstitial particles, whose intensity is proportional to defect density. Therefore, the higher ratio ($I_{DL}/I_{NBE}$) of DL emission to NBE emission means a higher relative content of defects in the sample. For $WO_3$ and $Bi_2O_3$, the relative PL ratios of $I_{DL}/I_{NBE}$ were calculated to be about 18.6 and 13.1, respectively. For the $Bi_2O_3/WO_3$ samples, there is no NBE emission lower than 400 nm, showing that more defects are present in the $Bi_2O_3/WO_3$ structure, and more electrons can participate in the redox reaction with the adsorbed oxygen.

The resistance and response of the semiconductor gas sensors are strongly dependent on the operating temperature, which provides heat energy to overcome the activation barriers of chemical adsorption and the reaction between the target gases and the sensor surface. Figure 4(a) shows the temperature-dependent responses of the gas sensors to 50 ppm TEA with the operating temperature ranging from 95 to 200 ℃. For the 0.4-$Bi_2O_3/WO_3$ sensor, the response rapidly increases from 2.1 to 9.2 upon increasing the operating temperature from 95 to 140 ℃. However, its values gradually decrease with the further increase in the operating temperature. Hereinafter, 140 ℃ is selected as the
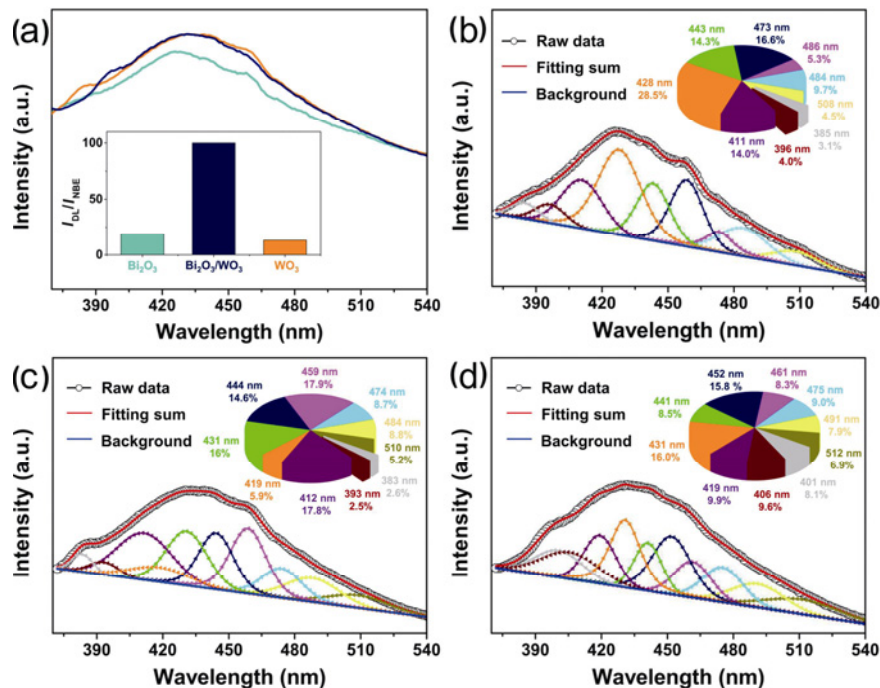


**Fig. 3** (a) PL spectra of $Bi_2O_3$, $WO_3$, and $Bi_2O_3/WO_3$. The inset shows the ratio of $I_{DL}/I_{NBE}$. Gaussian fittings of (b) $Bi_2O_3$, (c) $O_3$, and (d) $Bi_2O_3/WO_3$. The insets show the areal ratios of sub-peaks.

optimum operating temperature for the gas-sensing tests. As compared with the pure $WO_3$ sensor, whose peak response is 4.3 at 170 ℃, the sensor based on the 0.4-$Bi_2O_3$/$WO_3$ composite exhibits a much higher response (2.1-fold) to the TEA at a lower operating temperature (30 ℃-decrement), revealing the advantage of the $Bi_2O_3$/$WO_3$ composite in TEA detection. Herein, the performances of recent TEA sensors based on various metal oxides are compared [37–46], as summarized in Table 1. There is no doubt that the $Bi_2O_3$/$WO_3$ sensor possesses the ideal gas-sensing characteristics, including

high response and low power consumption. Furthermore, the resistance variations of the 0.4-$Bi_2O_3$/$WO_3$ sensor towards 50 ppm TEA were measured under different operating temperatures, as shown in Fig. 4(b). The sensor resistance gradually decreases with the increase in the temperature, mainly because the quantity and mobility of the carriers are influenced by the temperature.

For a clear comparison, the dynamic response curves of all the sensors at 140 ℃ towards 50 ppm TEA are shown in Fig. S7 in the ESM, and the response characteristics of all the sensors are summarized in
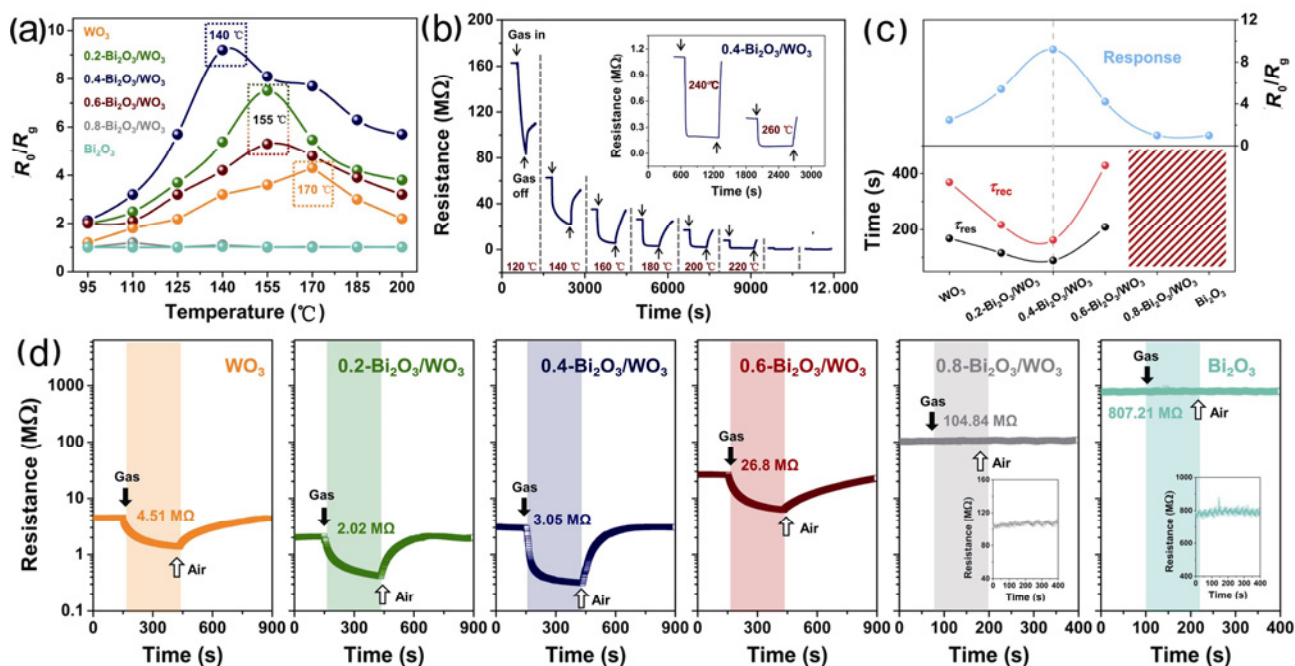


**Fig. 4** (a) Response of sensors to 50 ppm TEA under different operating temperatures. (b) Variations in resistance value of 0.4-$Bi_2O_3$/$WO_3$ sensor as a function of time towards 50 ppm TEA at 140 ℃. (c) Response value, response time, and recovery time and (d) corresponding transient plots as a function of $Bi_2O_3$ contents.

**Table 1   Comparison of TEA sensors based on various metal oxides**

| Sensing material | Operating temperature (℃) | Concerntration (ppm) | $R_0/R_g$ | Response/recovery time (s) | Ref. |
|---|---|---|---|---|---|
| Porous CuO | 230 | 100 | 7.7 | 21/150 | [37] |
| Hierarchical $NiCo_2O_4$ | 300 | 50 | 1.35 | 49/54 | [38] |
| $(Cu,Zn)Fe_2O_4$ | 160 | 50 | 6.77 | 58/136 | [39] |
| $Co_3O_4$@$MnO_2$ | 250 | 50 | 5 | 93/92 | [40] |
| $CuCrO_2$ nanoparticles | 140 | 100 | 5.2 | 90/120 | [41] |
| $Al_2O_3$/α-$Fe_2O_3$ | 250 | 50 | 10.6 | 1/17 | [42] |
| Hollow CuO | 260 | 100 | 4 | 21/25 | [43] |
| Hierarchical $Co_3O_4$/$WO_3$ | 300 | 1 | 2.6 | 13/152 | [44] |
| Hierarchical NiO/g-$C_3N_4$ | 280 | 500 | 20.36 | 157/350 | [45] |
| UV-activated ZnO–$SnO_2$ | 220 | 100 | 9.9 | 1.9/58 | [46] |
| Hierarchical $WO_3$ | 170 | 50 | 4.3 | 151/194 | This work |
| Hierarchical $Bi_2O_3$/$WO_3$ | 140 | 50 | 9.2 | 89/162 | This work |

Figs. 4(c) and 4(d). The 0.2-$Bi_2O_3$/$WO_3$ and 0.4-$Bi_2O_3$/$WO_3$ sensors exhibit baseline resistance of 2.02 and 3.05 MΩ, respectively, which are lower than that of pristine $WO_3$ (4.51 MΩ). Herein, the reduced resistance may be attributed to the band bending caused by the formation of the heterojunction between $Bi_2O_3$ and $WO_3$. The electrons from the conduction band of $WO_3$ are captured by the oxygen molecules adsorbed on the surface of $WO_3$ to form the chemically adsorbed oxygen and an electron depletion layer. The electron depletion layer will decrease the carrier concentration, increasing the baseline resistance of $WO_3$. Moreover, the electron transfer between the heterojunctions is accelerated, facilitating the reaction between the gas species and the gas-sensing materials, thus delivering a fast response and recovery of the sensor. During desorption, the baseline resistance returns to the initial values, indicating that the chemical reaction between the $Bi_2O_3$/$WO_3$ composite and the TEA is highly reversible. The above phenomenon was also demonstrated by the extended long-term stability and reproducibility tests, as well as the transient plots to different concentrations of the TEA. The resistance value of the composite is gradually decreased as the molar ratio of $Bi_2O_3$ increases, mainly because $Bi_2O_3$ provides a larger band gap, reducing the number of the electrons in the conduction band of the $Bi_2O_3$/$WO_3$ composite. The $Bi_2O_3$/$WO_3$ sensor exhibits no response at higher temperatures, which may be attributed to a combined effect of the instability of the TEA molecules to adsorb on the sensing materials and repulsion of these molecules with previously adsorbed oxygen molecules.

In practical applications, both the response value and response/recovery time are crucial parameters. In light of this, transient plots of the gas sensors based on the pure $WO_3$ and 0.4-$Bi_2O_3$/$WO_3$ composites were further studied at the optimal working temperature. As shown in Fig. 5(a), the response time of the 0.4-$Bi_2O_3$/$WO_3$ composite is shortened from 151 to 89 s, and the recovery time is shortened from 194 to 162 s. When the 0.4-$Bi_2O_3$/$WO_3$ composite is exposed to the TEA, the rise in the response implies that the materials exhibit the characteristics of an n-type semiconductor. When exposed to dry air, the response gradually decreases and eventually recovers to the initial value, indicating that the sensor response is stable. Furthermore, we evaluated the selectivity of the sensors based on the $WO_3$, $Bi_2O_3$, and $Bi_2O_3$/$WO_3$ composites towards 50 ppm of the interfering molecules including

methanol ($CH_4O$), ethanol ($C_2H_6O$), acetone ($C_3H_6O$), isopropanol ($C_3H_8O$), toluene ($C_7H_8$), ammonia ($NH_3$), and TEA ($C_6H_{15}N$). As shown in Fig. 5(b), all the 0.2-$Bi_2O_3$/$WO_3$, 0.4-$Bi_2O_3$/$WO_3$, and 0.6-$Bi_2O_3$/$WO_3$ sensors exhibit good selectivity. Especially, the response of the 0.4-$Bi_2O_3$/$WO_3$ sensor reaches about 9.2 towards the TEA while only 1–3.5 towards other gases. Herein, the high response and good selectivity of the composite sensor to the TEA is mainly attributed to the following two aspects: (1) the intrinsic acidic feature of $WO_3$, which is beneficial for the adsorption of the TEA molecule with N atom served as the Lewis basic site; (2) the formation of the heterojunction between $Bi_2O_3$ and $WO_3$, which promotes the charge transfer. As reported, the bond energy of O–H (methanol, ethanol), C=O (acetone), C–C (isopropanol), C=C (toluene), N–H (ammonia), and C–N (TEA) is 459, 799, 345, 610, 392, and 307 kJ/mol [47], respectively. The lower C–N bond energy facilitates the reaction activity of the TEA molecules among the above gases. As compared with other VOCs, the TEA molecule more easily loses the electron, and its N atom serves as the Lewis basic site, which is easily absorbed on the surface of acidic $WO_3$ [9].

In order to intuitively highlight the advantages of each sensor in different aspects and obtain the balance between the superior and the optimal working conditions, the performance parameters of $S$, $Q$, $1/T$, $1/\tau_{res}$, and $1/\tau_{rec}$ are multidimensionally compared in a wind rose diagram, as shown in Fig. 5(c). It is visible that the area of 0.4-$Bi_2O_3$/$WO_3$ is larger than the area of others, confirming that the optimal 0.4-$Bi_2O_3$/$WO_3$ sensor possesses a more balanced sensing performance for the TEA detection. Figure 5(d) illustrates the transient responses of the $WO_3$ and $Bi_2O_3$/$WO_3$ sensors upon exposure to various concentrations of the TEA at 140 ℃. With the increase in the TEA concentration, the response of the 0.4-$Bi_2O_3$/$WO_3$ sensor increases quickly from 2.8 at 0.5 ppm to 10.3 at 100 ppm. Meanwhile, the response can rapidly restore to its original baseline after the TEA is released. This result manifests that the 0.4-$Bi_2O_3$/$WO_3$ sensor is reproducible and has widely detection range from 0.5 to 100 ppm. The linear relationship between the sensor response and the gas concentration implies the advantage of the sensor in detecting low concentrations of the TEA (Fig. 5(e)). The detection limit ($D_L$) of the sensor can be extrapolated from the linear regime of the response values, which should be distinguishably differentiated
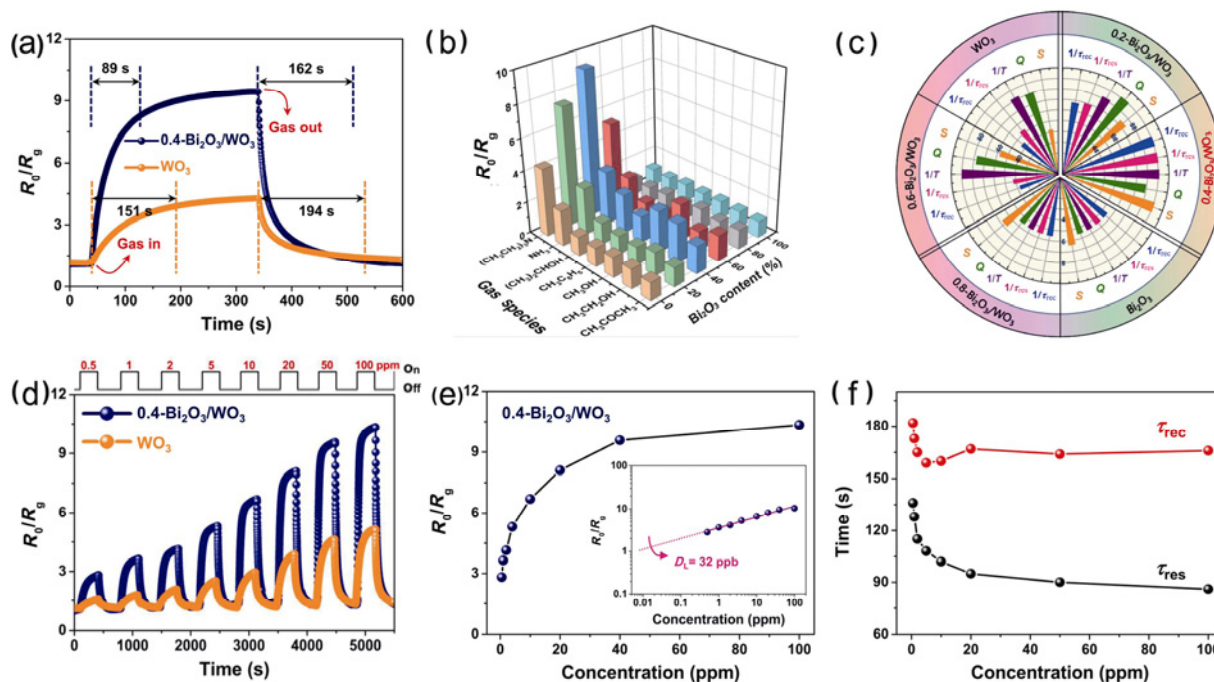
**Fig. 5** (a) Dynamic response–recovery curves for $WO_3$ and $Bi_2O_3/WO_3$ sensor to 50 ppm TEA. (b) Sensor responses towards 50 ppm of various target gases at 140 ℃. (c) Wind rose of response ($S$), selectivity ($Q$), and reciprocals of optimum operating temperature ($1/T$), response rate ($1/\tau_{res}$), and recovery rate ($1/\tau_{rec}$) for evaluating parameters of $Bi_2O_3$, $WO_3$, and $Bi_2O_3/WO_3$ sensors. (d) Transient plots of pure $WO_3$ and $Bi_2O_3/WO_3$ sensors to ppm-level TEA. (e) Relationship between sensor response and TEA concentration. The inset shows the corresponding dilogarithm curve. (f) Changes in response and recovery time for $Bi_2O_3/WO_3$ sensor along with TEA concentration.

from the background level. When the criterion for gas detection was set to $R_0/R_g > 1.5$, the theoretical $D_L$ of the 0.4-$Bi_2O_3/WO_3$ sensor was calculated to be 32 ppb, suggesting that the composite materials have the advantage for detecting the low-concentration TEA. With the increase of the TEA concentration, the response and recovery time basically presents a downward trend at the initial stage and remained unchanged thereafter (Fig. 5(f)), which may be the result of the nonuniform gas concentration after injection at the initial stage.

It is generally known that the gas-sensing performance of the semiconductor materials is critically influenced by relative humidity (RH). Herein, the humidity-dependent experiments of the $Bi_2O_3/WO_3$ sensor to 50 ppm TEA were conducted under different RHs in the range of 11%–97% RH (Fig. S8 in the ESM). As summarized in Fig. 6(a), the sensor response slightly declines about 11% along with the increase of the RH from 11% to 97%, which is apparently smaller than those reported in Refs. [15,30,38,42]. In addition, the anti-interference performance of the $Bi_2O_3/WO_3$ sensor was tested under three mixed gases of isopropanol, triethanolamine, and TEA (I—10 ppm: 10 ppm : 10 ppm; II—20 ppm : 20 ppm : 20 ppm; and III—50 ppm : 50

ppm : 50 ppm). As shown in Fig. 6(b), the sensor response decreases negligibly in the presence of the interfering molecules (triethanolamine and isopropanol), demonstrating the superiority of the $Bi_2O_3/WO_3$ sensor in the mixed gas detection. The long-term stability and reproducibility were also measured to evaluate the sensor performance, as shown in Figs. 6(c) and 6(d), respectively. No obvious variations in the response are observed during the test period of nearly 30 d and after running for 10 cycles, suggesting excellent stability and reproducibility of the $Bi_2O_3/WO_3$ gas sensor.

The synergistic effect between $WO_3$ and $Bi_2O_3$ plays a crucial role in improving the performance of the $Bi_2O_3/WO_3$ sensor. Firstly, the conductivity change of the composite upon the oxygen adsorption and gas reaction is believed to be a primary reason for the gas-sensing behavior. The band gaps of $WO_3$ and $Bi_2O_3$ are 2.78 and 2.83 eV, respectively. When they are in contact with each other, free electrons will flow from $Bi_2O_3$ to $WO_3$ to equate the Fermi levels, creating an electron depletion layer and an electron accumulation layer on the $Bi_2O_3$ side and $WO_3$ side, respectively (Fig. 7). When the sensor is exposed to an air atmosphere, the oxygen molecules are easily adsorbed on the surface
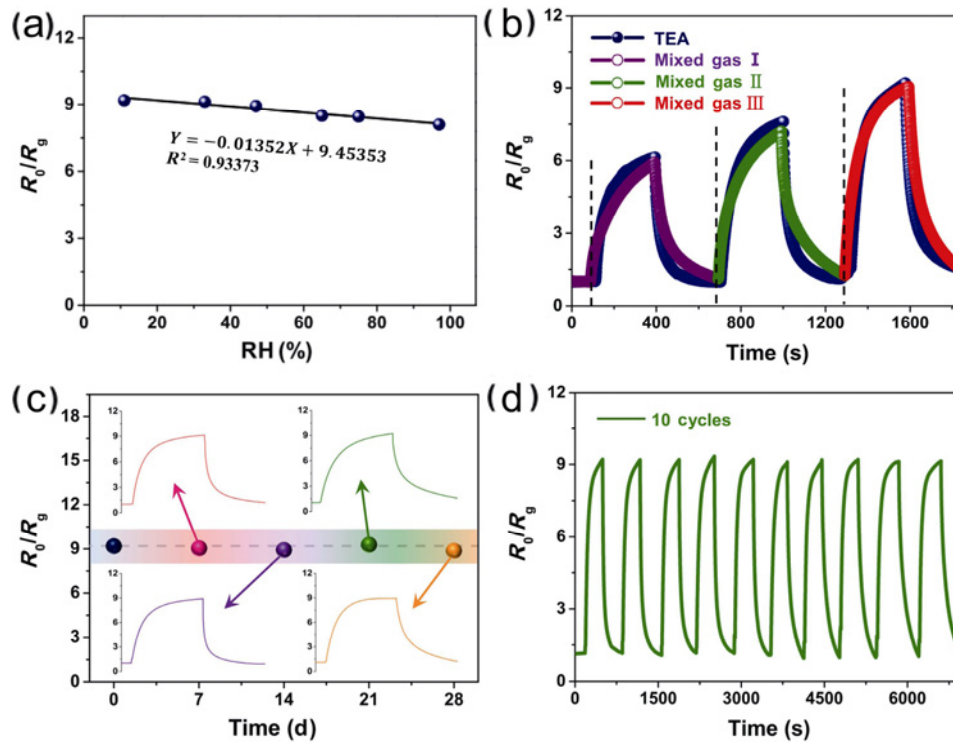
**Fig. 6** (a) Response values of $Bi_2O_3/WO_3$ sensor to 50 ppm TEA under various RHs. (b) Response curves of $Bi_2O_3/WO_3$ sensor to mixed gas of isopropanol, triethanolamine, and TEA. Mixed gas I—isopropanol : triethanolamine : TEA = 10 ppm : 10 ppm : 10 ppm; mixed gas II—isopropanol : triethanolamine : TEA = 20 ppm : 20 ppm : 20 ppm; mixed gas III—isopropanol : triethanolamine : TEA = 50 ppm : 50 ppm : 50 ppm. (c) Long-term stability and (d) reproducibility of $Bi_2O_3/WO_3$ sensor to 50 ppm TEA.
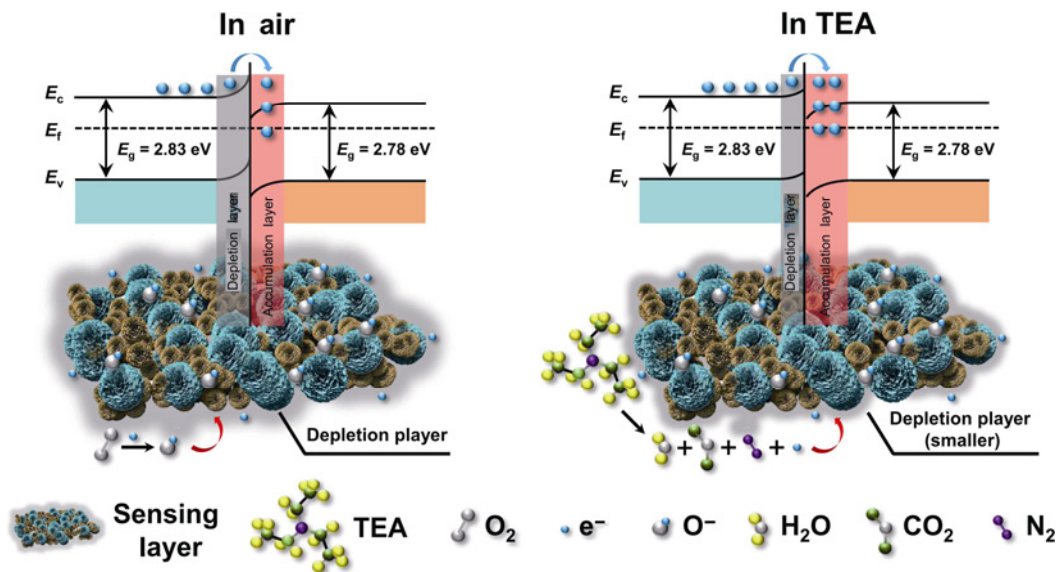


**Fig. 7** Energy-band diagrams and depletion layer changes of sensor based on $Bi_2O_3/WO_3$ composite when exposed to air and TEA. Note: $E_c$, $E_F$, and $E_v$ represent the energies at conduction band, Fermi level, and valence band, respectively.

of the $Bi_2O_3/WO_3$ composite to generate the oxygen-ion species (predominantly exist in the form of $O^-$), which increases the thickness of the depletion layer. Upon exposure to the TEA gas at 140 ℃, the trapped electrons are released to the composite by the reaction between the TEA molecules and chemisorbed oxygen species ($C_6H_{15}N + O^- \rightarrow CO_2 + N_2 + H_2O + e^-$), which decreases the electron depletion layer and results in a sharp decline in the resistance as observed. Secondly, the reactive sites are relatively increased by

the defects in the composite (Fig. 3), which accelerates the electron transfer and uplifts band bending for the electrons to pass through the electron depletion layer. Additionally, the rational design of a hierarchical structure guarantees abundant channels for the gas adsorption and desorption. The as-formed slit-like pores efficiently increase the contact region, facilitate the gas molecules to diffuse and interact with the composite, and thus advance the sensor performance.

## 4    Conclusions

In summary, the advanced $Bi_2O_3/WO_3$ composite has been successfully synthesized through a combination of the hydrothermal–ultrasonic procedure followed by the thermal treatment. Owing to the formation of the heterojunctions, the composite possesses decreased band gap and increased defect content, which is confirmed by the UV–Vis and PL analysis, respectively. Benefiting from the abundant slit-like pores, desirable defect features, and amplification effect of the heterojunctions between $WO_3$ and $Bi_2O_3$, the composite sensor shows a distinctive response of 0.5–2.8 ppm TEA, which meets up with the threshold value of toxic TEA concentration established by the OSHA. As compared with pristine $WO_3$ sensor, the composite sensor demonstrates faster response/recovery time (1.7-fold/1.2-fold), higher response (2.1-fold), and lower power consumption (30 ℃-decrement). In addition, the composite sensor exhibits the long-term stability, reproducibility, and negligible response towards the interfering molecules, indicating the promising potential of the $Bi_2O_3/WO_3$ heterojunction in the anti-interference detection of the low-concentration TEA in real applications. The novel design of the $Bi_2O_3/WO_3$ composite in this work shows great promise for rationally designing the advanced semiconductor gas sensors by utilizing the interfacial energy barriers of the hierarchical metal oxides.

## Author contributions

Mingxin Zhang: investigation, data curation, visualization, formal analysis, writing original draft, and writing—review & editing. Kai Liu: investigation, validation, and writing-review & editing. Xingmin Zhang: data curation. Bingbing Wang: resources and writing—review & editing. Xinru Xu: investigation. Xinxin Du: resources and investigation. Chao Yang: methodology and writing—review & editing.

Kewei Zhang: conceptualization, methodology, resources, writing—review & editing, supervision, and funding acquisition.

## Declaration of competing interest

The authors have no competing interests to declare that are relevant to the content of this article.

## Electronic Supplementary Material

Supplementary material is available in the online version of this article at https://doi.org/10.1007/s40145-022-0652-9.

## References

[1]    Gui YH, Tian K, Liu JX, *et al*. Superior triethylamine detection at room temperature by {−112} faceted $WO_3$ gas sensor. *J Hazard Mater* 2019, **380**: 120876.

[2]    Bai SL, Han JY, Han N, *et al*. An α-$Fe_2O_3$/NiO p–n hierarchical heterojunction for the sensitive detection of triethylamine. *Inorg Chem Front* 2020, **7**: 1532–1539.

[3]    Sun Y, Dong Z, Zhang D, *et al*. The fabrication and triethylamine sensing performance of In-MIL-68 derived $In_2O_3$ with porous lacunaris structure. *Sens Actuat B-Chem* 2021, **326**: 128791.

[4]    Liu JJ, Zhang LY, Fan JJ, *et al*. Semiconductor gas sensor for triethylamine detection. *Small* 2022, **18**: 2104984.

[5]    Gu FB, Cui YZ, Han DM, *et al*. Atomically dispersed Pt (II) on $WO_3$ for highly selective sensing and catalytic oxidation of triethylamine. *Appl Catal B Environ* 2019, **256**: 117809.

[6]    Li GJ, Ma ZH, Hu QM, *et al*. PdPt nanoparticle-functionalized α-$Fe_2O_3$ hollow nanorods for triethylamine sensing. *ACS Appl Nano Mater* 2021, **4**: 10921–10930.

[7]    Li ZS, Liu XH, Zhou M, *et al*. Plasma-induced oxygen vacancies enabled ultrathin ZnO films for highly sensitive detection of triethylamine. *J Hazard Mater* 2021, **415**: 125757.

[8]    Xu K, Zhan CY, Zhao W, *et al*. Tunable resistance of MOFs films via an anion exchange strategy for advanced

gas sensing. *J Hazard Mater* 2021, **416**: 125906.

[9] He M, Xie LL, Luo GF, *et al*. Flexible fabric gas sensors based on PANI/WO₃ p–n heterojunction for high performance NH₃ detection at room temperature. *Sci China Mater* 2020, **63**: 2028–2039.

[10] Zhang YH, Wang CN, Gong FL, *et al*. Ultra-sensitive triethylamine sensors based on oxygen vacancy-enriched ZnO/SnO₂ micro-camellia. *J Mater Chem C* 2021, **9**: 6078–6086.

[11] Kitney SP, Sajedin SM, Rocher V, *et al*. Silicon diimide gel as an efficient stationary phase in thin layer chromatography for acid-sensitive organic compounds. *Chem Commun* 2017, **53**: 11080–11082.

[12] Mirzaei A, Leonardi SG, Neri G. Detection of hazardous volatile organic compounds (VOCs) by metal oxide nanostructures-based gas sensors: A review. *Ceram Int* 2016, **42**: 15119–15141.

[13] Zhang Y, Han S, Wang MY, *et al*. Electrospun Cu-doped In₂O₃ hollow nanofibers with enhanced H₂S gas sensing performance. *J Adv Ceram* 2022, **11**: 427–442.

[14] Jo YK, Jeong SY, Moon YK, *et al*. Exclusive and ultrasensitive detection of formaldehyde at room temperature using a flexible and monolithic chemiresistive sensor. *Nat Commun* 2021, **12**: 4955.

[15] Bai SL, Zhang KW, Zhao YY, *et al*. rGO decorated NiO–BiVO₄ heterojunction for detection of NO₂ at low temperature. *Sens Actuat B-Chem* 2021, **329**: 128912.

[16] Zhang MX, Yang C, Zhang ZQ, *et al*. Tungsten oxide polymorphs and their multifunctional applications. *Adv Colloid Interface Sci* 2022, **300**: 102596.

[17] Guo MM, Luo N, Chen Y, *et al*. Fast-response MEMS xylene gas sensor based on CuO/WO₃ hierarchical structure. *J Hazard Mater* 2022, **429**: 127471.

[18] Li QQ, Han N, Zhang KW, *et al*. Novel p–n heterojunction of BiVO₄/Cu₂O decorated with rGO for low concentration of NO₂ detection. *Sens Actuat B-Chem* 2020, **320**: 128284.

[19] Wei ZJ, Zhou Q, Zeng W. Hierarchical WO₃–NiO microflower for high sensitivity detection of SF₆ decomposition byproduct H₂S. *Nanotechnology* 2020, **31**: 215701.

[20] Chen SF, Hu YF, Meng SG, *et al*. Study on the separation mechanisms of photogenerated electrons and holes for composite photocatalysts g-C₃N₄–WO₃. *Appl Catal B Environ* 2014, **150–151**: 564–573.

[21] Zhang JF, Hu YF, Jiang XL, *et al*. Design of a direct Z-scheme photocatalyst: Preparation and characterization of Bi₂O₃/g-C₃N₄ with high visible light activity. *J Hazard Mater* 2014, **280**: 713–722.

[22] Wei YL, Rong B, Chen X, *et al*. Porous and visible-light-driven p–n heterojunction constructed by Bi₂O₃ nanosheets and WO₃ microspheres with enhanced photocatalytic performance. *Sep Purif Technol* 2021, **256**: 117815.

[23] Khan I, Abdalla A, Qurashi A. Synthesis of hierarchical WO₃ and Bi₂O₃/WO₃ nanocomposite for solar-driven water splitting applications. *Int J Hydrogen Energ* 2017, **42**: 3431–3439.

[24] Liu W, Zheng Y, Wang Z, *et al*. Ultrasensitive exhaled breath sensors based on anti-resonant hollow core fiber with *in situ* grown ZnO–Bi₂O₃ nanosheets. *Adv Mater Interfaces* 2021, **8**: 2001978.

[25] Bang JH, Choi MS, Mirzaei A, *et al*. Selective NO₂ sensor based on Bi₂O₃ branched SnO₂ nanowires. *Sens Actuat B-Chem* 2018, **274**: 356–369.

[26] Devi GS, Manorama SV, Rao VJ. SnO₂/Bi₂O₃: A suitable system for selective carbon monoxide detection. *J Electrochem Soc* 1998, **145**: 1039–1044.

[27] Bai SL, Zhang KW, Luo RX, *et al*. Sonochemical synthesis of hierarchically assembled tungsten oxides with excellent NO₂-sensing properties. *Mater Lett* 2013, **111**: 32–34.

[28] Bai SL, Zhang KW, Wang LS, *et al*. Synthesis mechanism and gas-sensing application of nanosheet-assembled tungsten oxide microspheres. *J Mater Chem A* 2014, **2**: 7927–7934.

[29] Wang P, Wang SZ, Kang YR, *et al*. Cauliflower-shaped Bi₂O₃–ZnO heterojunction with superior sensing performance towards ethanol. *J Alloys Compd* 2021, **854**: 157152.

[30] Zhang MX, Zhao ZH, Hui B, *et al*. Carbonized polymer dots activated hierarchical tungsten oxide for efficient and stable triethylamine sensor. *J Hazard Mater* 2021, **416**: 126161.

[31] Bai SL, Zhang KW, Sun JH, *et al*. Surface decoration of WO₃ architectures with Fe₂O₃ nanoparticles for visible-light-driven photocatalysis. *CrystEngComm* 2014, **16**: 3289–3295.

[32] Bai SL, Zuo Y, Zhang KW, *et al*. WO₃–ZnFe₂O₄ heterojunction and rGO decoration synergistically improve the sensing performance of triethylamine. *Sens Actuat B-Chem* 2021, **347**: 130619.

[33] Zhu GL, Yang W, Lv WQ, *et al*. Facile electrophoretic deposition of functionalized Bi₂O₃ nanoparticles. *Mater Des* 2017, **116**: 359–364.

[34] Yang XY, Zhang YM, Wang YL, *et al*. Hollow β-Bi₂O₃@CeO₂ heterostructure microsphere with controllable crystal phase for efficient photocatalysis. *Chem Eng J* 2020, **387**: 124100.

[35] Zhang J, Ma Y, Du YL, *et al*. Carbon nanodots/WO₃ nanorods Z-scheme composites: Remarkably enhanced photocatalytic performance under broad spectrum. *Appl Catal B Environ* 2017, **209**: 253–264.

[36] Lu HJ, Hao Q, Chen T, *et al*. A high-performance Bi₂O₃/Bi₂SiO₅ p–n heterojunction photocatalyst induced by phase transition of Bi₂O₃. *Appl Catal B Environ* 2018, **237**: 59–67.

[37] Du XX, Tian WL, Zhang ZQ, *et al*. Defect promoted photothermoelectric effect in densely aligned ZnO nanorod arrays for self-powered position-sensitive photodetection. *J Materiomics* 2022, **8**: 693–701.

[38] Wu YP, Zhou W, Dong WW, *et al*. Temperature-controlled synthesis of porous CuO particles with different morphologies for highly sensitive detection of triethylamine. *Cryst Growth Des* 2017, **17**: 2158–2165.

[39] Yang C, Xu YS, Zheng LL, *et al*. Hierarchical NiCo₂O₄ microspheres assembled by nanorods with p-type response for detection of triethylamine. *Chin Chem Lett* 2020, **31**: 2077–2082.

[40] Yang J, Li X, Wu J, *et al*. Yolk–shell (Cu,Zn)Fe$_2$O$_4$ ferrite nano-microspheres with highly selective triethylamine gas-sensing properties. *Dalton Trans* 2020, **49**: 14475–14482.

[41] Liang Y, Yang Y, Xu K, *et al*. Controllable preparation of faceted Co$_3$O$_4$ nanocrystals@MnO$_2$ nanowires shish-kebab structures with enhanced triethylamine sensing performance. *Sens Actuat B-Chem* 2020, **304**: 127358.

[42] Liu H, Cao X, Wu H, *et al*. Innovative development on a p-type delafossite CuCrO$_2$ nanoparticles based triethylamine sensor. *Sens Actuat B-Chem* 2020, **324**: 128743.

[43] Guo LL, Wang C, Kou XY, *et al*. Detection of triethylamine with fast response by Al$_2$O$_3$/α-Fe$_2$O$_3$ composite nanofibers. *Sens Actuat B-Chem* 2018, **266**: 139–148.

[44] Geng WC, Ma ZY, Zhao YJ, *et al*. The self-assembly of octahedral Cu$_x$O and its triethylamine-sensing properties. *Sens Actuat B-Chem* 2020, **312**: 128014.

[45] Gui YH, Yang LL, Tian K, *et al*. P-type Co$_3$O$_4$ nanoarrays decorated on the surface of n-type flower-like WO$_3$ nanosheets for high-performance gas sensing. *Sens Actuat B-Chem* 2019, **288**: 104–112.

[46] Li XZ, Wang Y, Tian WD, *et al*. Graphitic carbon nitride nanosheets decorated flower-like NiO composites for high-performance triethylamine detection. *ACS Omega* 2019, **4**: 9645–9653.

[47] Yang TY, Gu KK, Zhu MM, *et al*. ZnO–SnO$_2$ heterojunction nanobelts: Synthesis and ultraviolet light irradiation to improve the triethylamine sensing properties. *Sens Actuat B-Chem* 2019, **279**: 410–417.

[48] Song XP, Xu Q, Xu HY, *et al*. Highly sensitive gold-decorated zinc oxide nanorods sensor for triethylamine working at near room temperature. *J Colloid Interface Sci* 2017, **499**: 67–75.